JPE 16-1-33

http://dx.doi.org/10.6113/JPE.2016.16.1.319
ISSN(Print): 1598-2092 / ISSN(Online): 2093-4718

On DC-Side Impedance Frequency Characteristics Analysis and DC Voltage Ripple Prediction under Unbalanced Conditions for MMC-HVDC System Based on Maximum Modulation Index

Yiqi Liu†, Qichao Chen*, Ningning Li*, Bing Xie*, Jianze Wang*, and Yanchao Ji*

†,*School of Electrical Engineering and Automation, Harbin Institute of Technology, Harbin, China

Abstract

In this study, we first briefly introduce the effect of circulating current control on the modulation signal of a modular multilevel converter (MMC). The maximum modulation index is also theoretically derived. According to the optimal modulation index analysis and the model in the continuous domain, different DC-side output impedance equivalent models of MMC with/without compensating component are derived. The DC-side impedance of MMC inverter station can be regarded as a series $xR + yL + zC$ branch in both cases. The compensating component of the maximum modulation index is also related to the DC equivalent impedance with circulating current control. The frequency characteristic of impedance for MMC, which is observed from its DC side, is analyzed. Finally, this study investigates the prediction of the DC voltage ripple transfer between two-terminal MMC high-voltage direct current systems under unbalanced conditions. The rationality and accuracy of the impedance model are verified through MATLAB/Simulink simulations and experimental results.

Key words: DC voltage ripple, Fault prediction, High-voltage direct current, Impedance prediction, Maximum modulation index, Modular multilevel converter

I. INTRODUCTION

An interfacing converter plays an important role in the integration of renewable energy into modern electric grids [1]–[3]. It functions as the bridge to connect the source, load, and grid. The modular multilevel converter (MMC) is the most suitable converter for HVDC transmission [4], [5], medium- or high-voltage motor drive applications [6], [7], and electric railway supplies because of its recognized features in

terms of modularity, reliability, and efficiency, [8]. A switching process of MMC can affect the response of AC/DC link under some disturbances, and a circulating current that flows within its three-phase units is generated. Given that the circulating current control increases the converter, power loss results in a complex and non-linear system phenomenon or even instability issues [9]–[11].

New modulation methods have been proposed to suppress the circulating current and to eliminate harmonics by avoiding its influence on the AC terminal. PWM methods, including carrier-phase-shifted PWM [12], submodule (SM) unified PWM [13], and selective harmonic elimination method [14], share some common features, such as high switching frequency, large switching losses, and complex implementation process. Unlike the aforementioned methods, the nearest level modulation (NLM) method [15] does not need a complex calculation of the trigger angles. Therefore, NLM is the simplest and the most practical modulation method for MMC.

The upper and lower arm voltage references of MMC consist of constant DC voltage and fundamental frequency component [16]. Thus, the restriction of arm voltage reference is determined by the value of the modulation index. At the same time, the circulating current control employs additional component into the arm voltage reference, which influences

Manuscript received May 3, 2015; accepted Jul. 31, 2015
Recommended for publication by Associate Editor Kyeon Hur.
†Corresponding Author: liuyq0925@126.com
Tel: +86-15645073688, Harbin Institute of Technology
*School of Electrical Engineering and Automation, Harbin Institute of Technology, China

the characteristics of DC-side impedance and maximum modulation index of MMC. Hence, overmodulation can be avoided, and DC voltage utilization is reduced. Preceding research focused on circulating current suppression and on reducing DC voltage ripple distortion. However, the effects of the DC impedance model and its frequency characteristics are still not fully explained to the approaches of predicting any possible resonance problems, which are important in exploring the impedance of the converter on the DC side. The DC voltage ripple transfer is also a challenge from the fault converter to other converters.

This study aims to derive the maximum modulation index and DC-side equivalent impedance of MMC considered in the HVDC system. A detailed model of MMC is first presented, and an analysis of the modulation index to DC-side impedance frequency characteristic is provided. When the fault occurs in a terminal of the two-terminal MMC-HVDC system, the effect of this terminal on the other terminal is studied with DC-side impedance model. Thus, the DC voltage ripple propagation between the two terminals in HVDC system under unbalanced conditions is predicted. Finally, the simulation and experimental results verify the validity of the derived model and DC voltage ripple prediction results.

II. Basic Configuration and Control Method for MMC

A. Basic Configuration

The currents, voltage, and insertion indices must be defined to perform the following calculation. Fig. 1 shows the configuration of MMC [17]. A three-phase MMC consists of three-phase legs with upper and lower arms. Each arm has a series-connected N SMs and inductor L_0 and arm equivalent resistance R_0. A single SM has two switching states (i.e., on and off) and one capacitor (i.e., C_{sub}), and the corresponding output voltage of SM is v_{cp} or v_{cn} in the upper or lower arm. The subscript "p" denotes the upper arm, whereas "n" denotes the lower arm. The equivalent circuit of the single MMC under steady state is depicted in Fig. 1, where v_j (j = a, b, c) is the converter output voltage of phase j. The reference for i_j is the corresponding line current. Thus, the inserted voltage and capacitor currents are proportional to the insertion indices in each other arm. Similarly, the voltage v_p (v_n) can be obtained by multiplying the insertion index with the capacitor voltage, which is shown as

$$v_{p(n)} = \mu_{p(n)} \cdot v_{cp(n)} \quad , \tag{1}$$

where μ_p and μ_n are the inserted SM numbers to the total SM numbers in each arm, and they can be expressed as in Equ. (2):

$$\mu_{p(n)} = \frac{N}{V_{dc}}\left(\frac{V_{dc}}{2} \mp v_j\right), \tag{2}$$

where V_{dc} is the DC link voltage, and N is the assumption total number of SMs.

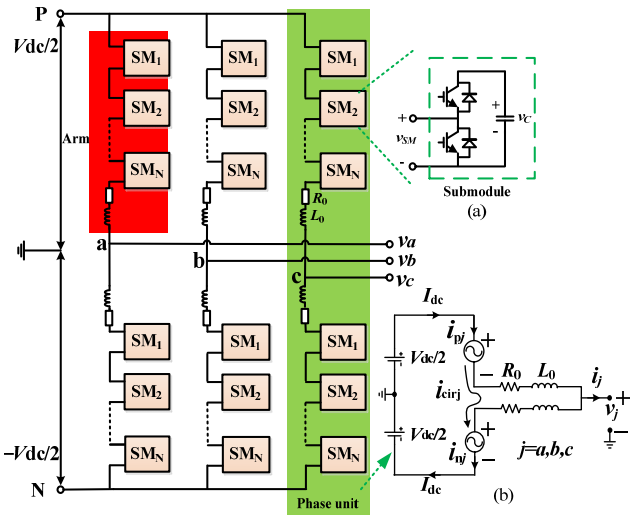

Fig. 1. Circuit configuration of MMC.

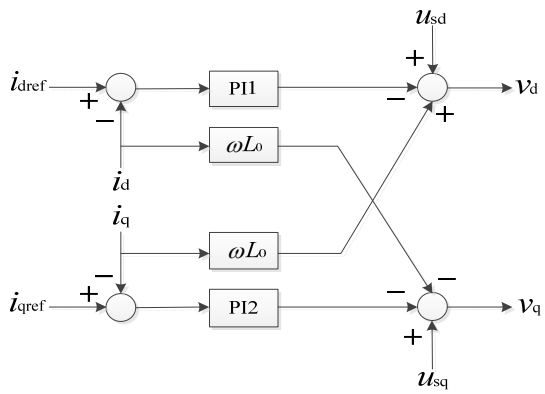

Fig. 2. Control diagram of MMC.

According to the single-phase unit circuit in Fig. 1, the AC-side voltage can be described with the following based on Kirchhoff's law:

$$\frac{V_{dc}}{2} - v_{pj} - \left(L_0 \frac{di_{pj}}{dt} + R_0 i_{pj}\right) = v_j \,, \tag{3a}$$

$$\frac{V_{dc}}{2} - v_{nj} - \left(L_0 \frac{di_{nj}}{dt} + R_0 i_{nj}\right) = -v_j \,. \tag{3b}$$

B. Control Method

The active and reactive power are in control because the outer control loop provides the references for the inner current control loop [18]. The inner current control loop aims to regulate the d-q axis currents, and its output is the electromotive force v_{dq}. The disturbance inputs can be cancelled with feedforward compensation u_{sdq} [19]. The modulation and input voltage balancing control is presented with Equ. (4), and the diagram of inverter control system is shown in Fig. 2. Finally, the main control parameters are selected as follows: $k_p = 8.05 \times 10^{-4}$, $k_i = 0.115$, ω = 60 Hz.

The corresponding closed loop root locus is illustrated in Fig. 3. The proportional control parameter k_i (k_p) increases when k_p (k_i) is constant. The closed loop dominant poles P_1 and P_2 also move toward the imaginary axis. Hence, the stability of the control system can be guaranteed.

$$v_d = u_{sd} + \omega L_0 i_q - G_{PI}(i_{dref} - i_d) \tag{4a}$$

$$v_q = u_{sq} - \omega L_0 i_d - G_{PI}(i_{qref} - i_q) \tag{4b}$$

The circulating current flows among the three phases of MMC. Thus, it increases the RMS current, thereby increasing the power loss on the devices in SMs. According to [20], an extra compensating component (n_{cir}) is added to the insertion indices n_p and n_n. Hence, insertion indices can be expressed as in Equ. (5).

$$n_p = \frac{N}{V_{dc}}\left(\frac{V_{dc}}{2} - v_j\right) + n_{cir} \tag{5a}$$

$$n_n = \frac{N}{V_{dc}}\left(\frac{V_{dc}}{2} + v_j\right) + n_{cir} \tag{5b}$$

III. Maximum Modulation Index Calculation for MMC

The difference of charge and discharge of the phase unit SM capacitor of MMC leads to an imbalance in SM capacitor voltage, thereby reducing service life and causing circulating current power loss. These negative effects can be avoided by introducing a new insertion index μ_{cir} into the arm voltage reference to offset the capacitor voltage of the SM.

$$\mu_{cir} = n_{cir} \cdot \mathrm{N} \tag{6}$$

According to Equ. (3), the AC-side voltage can be expressed as

$$\frac{V_{dc}}{2} - v_{pj} - \left(L_0 \frac{di_{pj}}{dt} + R_0 i_{pj} - \mu_{cir} v_{cp}\right) = v_j\,, \tag{7a}$$

$$\frac{V_{dc}}{2} - v_{nj} - \left(L_0 \frac{di_{nj}}{dt} + R_0 i_{nj} - \mu_{cir} v_{cn}\right) = -v_j\,. \tag{7b}$$

On the basis of Equ. (7), the DC-side voltage equivalent model can be written as

$$V_{dc} = v_{pj} + v_{nj} + L_0 \frac{d(i_{pj} + i_{nj})}{dt} + R_0(i_{pj} + i_{nj}) - \mu_{cir}(v_{cp} + v_{cn})\,. \tag{8}$$

In MMC, the fundamental component and second-order frequency make obtaining the unbalanced voltage and the insertion indices difficult. Given that R_0 is small, the following can be obtained:

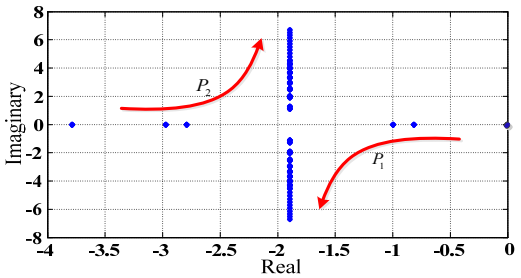

(a) k_p is constant.

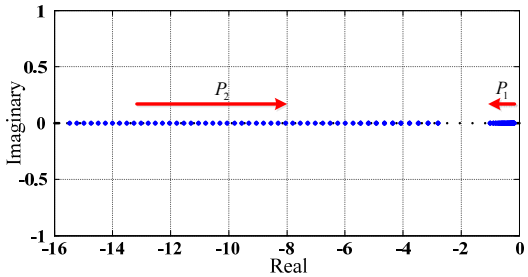

(b) k_i is constant.

Fig. 3. Closed-loop root locus of the control diagram.

$$V_{dc} = \frac{N}{2}(v_{cp} + v_{cn}) + \frac{N v_j}{V_{dc}}(v_{cn} - v_{cp}) - \mu_{cir}(v_{cp} + v_{cn})\,. \tag{9}$$

SM capacitance C is generally large enough to render the deviation of each capacitor voltage ripple, which is very small. Meanwhile, the AC-side current, DC-side SM capacitor voltage, and circulating current can be controlled. Therefore, the SM capacitor voltage ripple can be neglected in a steady-state system with the following assumptions:

$$V_{dc} \approx N \cdot \frac{v_{cp} + v_{cn}}{2}\,, \tag{10}$$

where $0.5(v_{cp} + v_{cn})$ is the steady-state values for the average voltage of the upper and lower arms.

The insertion index n_{cir} can be calculated as follows by substituting Equ. (10) into Equ. (9):

$$n_{cir} = \frac{v_j}{V_{dc}} \cdot \frac{v_{cn} - v_{cp}}{v_{cn} + v_{cp}}\,. \tag{11}$$

According to the equivalent circuit of MMC at the DC and AC sides in [16], the DC-side active power and AC-side active power can be expressed as in Equ. (12):

$$P_{dc} = V_{dc} i_{dc}\,, \tag{12a}$$

$$P_j = v_j i_j \cos\varphi\,. \tag{12b}$$

At the same time, $P_{dc} = P_{ac}$ can be obtained by neglecting the power loss of the converter with the power balance at the DC and AC terminals, which keep the balance of energy exchange between the phase leg and DC link. The average value of the circulating current i_{dc} represents the current that must flow through the phase leg to keep a certain power flow

on the AC side [21]. i_{dc} can be obtained by solving Equ. (12).

$$i_{dc} = \frac{M}{4} I_j \cos\varphi , \tag{13}$$

where M is the modulation index, which is defined as $2v_j/V_{dc}$. φ represents the power angle between AC phase voltage and current.

The SM capacitor voltage of the upper and lower arm can be expressed as

$$C\frac{dv_{cp(n)}}{dt} = n_{p(n)} i_{p(n)j} . \tag{14}$$

The sum of the SM capacitor voltages and the differences of upper and lower arms are shown in Equs. (15) and (16) by combining Equs. (5) and (11)–(14).

$$v_{cp} + v_{cn} = \frac{2V_{dc}}{N} - \frac{M}{8C\omega} I_j \sin(2\omega t - \varphi) = v_c^+ , \tag{15}$$

$$v_{cn} - v_{cp} = \frac{I_j[\sin\varphi\cos(\omega t) - (1-\frac{M^2}{2})\cos\varphi\sin(\omega t)]}{2\omega C} = v_c^- . \tag{16}$$

n_{cir} can be obtained as in Equ. (17) by inserting Equs. (15) and (16) into Equ. (11):

$$n_{cir} = \frac{NM}{16\omega C V_{dc}} I_j[(\frac{3}{2} - \frac{M^2}{2})\sin(2\omega t)\cos\varphi - \frac{3}{2}\cos(2\omega t)\sin\varphi - \sin\varphi] . \tag{17}$$

The insertion index for the upper and lower arms can be rewritten as Equ. (18) by combining Equs. (6) and (17), which is shown as

$$n'_p = \frac{1}{2} - \frac{M}{2}\cos\omega t + \frac{NM}{16\omega C V_{dc}} I_j[(\frac{3}{2} - \frac{M^2}{2})\sin(2\omega t)\cos\varphi - \frac{3}{2}\cos(2\omega t)\sin\varphi - \sin\varphi] , \tag{18a}$$

$$n'_n = \frac{1}{2} + \frac{M}{2}\cos\omega t + \frac{NM}{16\omega C V_{dc}} I_j[(\frac{3}{2} - \frac{M^2}{2})\sin(2\omega t)\cos\varphi - \frac{3}{2}\cos(2\omega t)\sin\varphi - \sin\varphi] , \tag{18b}$$

where $n'_p + n'_n = 1$, and insertion index should satisfy

$$0 \le n'_p(n'_n) \le 1 . \tag{19}$$

From these results, the maximum and minimum of the upper and lower arm insertion indices are obtained when cos(φ) equals its minimum value:

$$n'_p(max) = 0.5 - (0.5 - 0.428\varepsilon)M , \tag{20a}$$

$$n'_p(min) = 0.5 - (0.5 + 0.428\varepsilon)M , \tag{20b}$$

$$n'_n(max) = 0.5 + (0.5 + 0.428\varepsilon)M , \tag{21a}$$

$$n'_n(min) = 0.5 + (0.5 - 0.428\varepsilon)M , \tag{21b}$$

where ε is the maximum relative SM capacitor voltage ripple. The relationship is shown as follows by letting the capacitor have a relative voltage deviation (i.e., ε around its reference value v_c,):

$$v_c(1-\varepsilon) \le v_c \le v_c(1+\varepsilon). \tag{22}$$

The capacitor energy per SM is presented with Equ. (23) [22]

$$W_{sub}(v_c) = \frac{1}{2} C_{sub} v_c^2 = \frac{1}{6\varepsilon} \cdot \frac{P_s}{M \cdot N \cdot \omega} \left(1 - (\frac{M\cos\varphi}{2})^2\right)^{\frac{3}{2}} , \tag{23}$$

where P_s is the AC-side output power of the converter, and φ is the power factor angle. According to [23], the maximum reactive power is generally defined as half of the maximum active power. Therefore, the power factor at the full apparent power is 0.866, and the maximum capacitor voltage ripple ε can be expressed as in Equ. (24):

$$\varepsilon = 0.73 \cdot \frac{1}{C_{sub}} \cdot \frac{1}{4\omega} \cdot I_j \cdot \frac{N}{V_{dc}} . \tag{24}$$

The constraint of the modulation index can be obtained as follows by combining Equs. (19) to (21):

$$M \le \frac{1}{1 + 0.856\varepsilon} . \tag{25}$$

The preceding discussion indicates that the insertion index is related to the operating conditions M, I_j, φ, and V_{dc} and system parameters C and N. The maximum modulation index is smaller than 1. It is also related to SM capacitor voltage ripple.

IV. DC-SIDE IMPEDANCE FREQUENCY CHARACTERISTICS AND VOLTAGE RIPPLE TRANSFER PREDICTION ANALYSIS

A. Impedance Frequency Characteristics Analysis

According to Equs. (5) and (14), expressing the SM voltages as follows is reasonable:

$$v_{cp} = \frac{1}{C}\int(\frac{1}{2} i_{pj} - \frac{v_j}{V_{dc}} i_{pj} + n_{cir} i_{pj})dt , \tag{26a}$$

$$v_{cn} = \frac{1}{C}\int(\frac{1}{2} i_{nj} + \frac{v_j}{V_{dc}} i_{nj} + n_{cir} i_{nj})dt . \tag{26b}$$

The sum of the three-phase arm current is the direct current:

$$\sum_{k=1}^{3} i_{pj} = \sum_{k=1}^{3} i_{nj} = i_{dc} . \tag{27}$$

Then, the sum and the difference of the upper and lower arms of the SM capacitor voltage of the phase unit can be

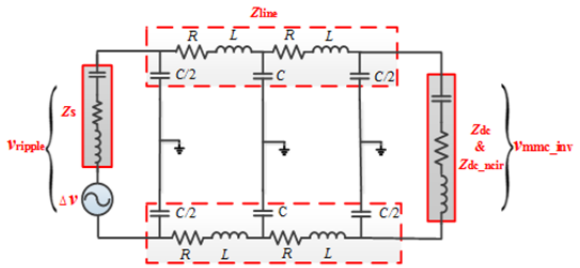

Fig. 4. Equivalent inner impedance in the inverter side.

obtained

$$\sum_{k=1}^{3}(v_{cp}+v_{cn})=\frac{1}{C}\int(1+2n_{cir})i_{dc}dt\,, \tag{28}$$

$$\sum_{k=1}^{3}(v_{cn}-v_{cp})=\frac{1}{C}\int\frac{2v_j}{V_{dc}}i_{dc}dt\,. \tag{29}$$

According to Equs. (9) and (26) to (29),

$$V_{dc}=\frac{2}{3}R_0i_{dc}+\frac{2}{3}L_0\frac{di_{dc}}{dt}+\frac{N}{6C}[1+\frac{2n_{cir}(N-1-2n_{cir})}{N}]\int i_{dc}dt\,. \tag{30}$$

The balanced converter-side current is proved achievable in the system performance with both controllers in a two-terminal MMC-HVDC, whereas the second-order DC-side voltage ripple cannot be eliminated by the constant AC active power control scheme. To deal with this issue, the compensating component is inserted in this study instead of the traditional circulating current control and suppressing the second-order DC-side current under unbalanced conditions. The expression of DC-side equivalent impedance is related only to R_0, L_0, C, and n_{cir} through the small-signal perturbation frequency domain analysis of Equ. (30) [24], [25]. The DC equivalent impedance model of MMC in the frequency domain can be determined as follows:

$$Z_{dc\_cir}(f)=\frac{2R_0}{3}+j\left(\frac{4\pi fL_0}{3}-\frac{N}{12\pi fC}[1+\frac{2n_{cir}(N-1-2n_{cir})}{N}]\right). \tag{31}$$

The DC-side impedance frequency domain model without compensating component is a series of R_0, L_0, and C. It can be defined as

$$Z_{dc}(f)=\frac{2R_0}{3}+j(\frac{4\pi fL_0}{3}-\frac{N}{12\pi fC})\,. \tag{32}$$

The DC voltage ripple can be predictive by analyzing the DC-side impedance frequency characteristics and through system parameters R_0, L_0, C, and n_{cir}. Thus, the following equations can be derived based on Equs. (31) and (32):

$$f_{dc}=\frac{1}{4\pi}\sqrt{\frac{N}{CL_0}}\,, \tag{33}$$

$$f_{dc\_cir}=\frac{1}{4\pi}\sqrt{\frac{N}{CL_0}[1+\frac{2n_{cir}(N-1-2n_{cir})}{N}]}\,, \tag{34}$$

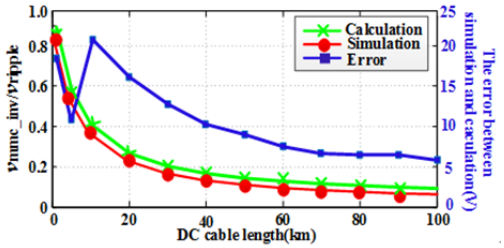

(a) Effect of DC cable length.

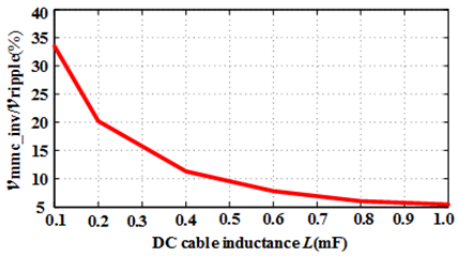

(b) Effect of DC cable inductance.

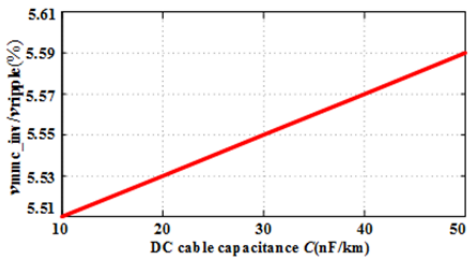

(c) Effect of DC cable capacitance.

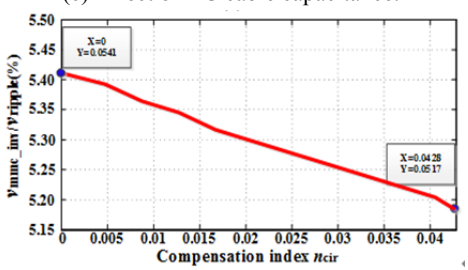

(d) Effect of compensation index.

Fig. 5. Effect of system parameters on v_{mmc_inv}/v_{ripple}.

where f_{dc} and f_{dc_cir} represent the DC-side equivalent impedance frequency with and without a compensating component, respectively. MMC DC-side impedance is changed between capacitive and inductive following the different values of R_0, L_0, C, and n_{cir}. The MMC performs as a capacitive impedance when $f < f_{dc}$ (f_{dc_cir}). By contrast, the MMC performs as inductive impedance.

B. DC Voltage Ripple Transfer Prediction

According to the preceding derivation of DC-side equivalent impedance for MMC, the equivalent circuit of HVDC system based on MMC can be obtained. An inverter with distorted DC voltage is applied instead of back-to-back HVDC system to avoid the low-frequency harmonics induced

by overmodulation during unbalanced system assuming that the DC voltage of the rectifier is constant. The equivalent impedance model of DC side is shown in Fig. 4, where Z_s is the internal impedance of the source, Z_{line} is the impedance of the power cable, which is represented by π model, and Z_{dc} is the equivalent impedance of the DC side of the inverter.

The induced ripple voltage is shown as v_{ripple} when faults occur in MMC-HVDC system. On the basis of the model of the equivalent impedance, the effect of the first side of the fault to the other side can be predicted. The effects of the length of the cable and its equivalent inductance and capacitance are discussed in the simulation. Fig. 5(a) illustrates that v_{mmc_inv}/v_{ripple} is reduced with the increasing length of the cable. The effect of internal inductance, capacitance, and compensating component n_{cir} on v_{mmc_inv}/v_{ripple} is further analyzed. The capability of fault transfer is reduced by increasing the equivalent inductance and capacitance while keeping the distance the same. A linear relationship can be determined with increasing capacitance.

V. Simulation Results and Experimental Verifications

A. Simulation Results

In Section IV, the equivalent of DC impedance is derived. The parameters related to DC-side equivalent impedance are obtained. The simulation model of a three-phase MMC-HVDC is also established in MATLAB/Simulink. The main circuit parameters of the simulation system are provided in Table I.

The steady-state values v_{c+}, v_{c-}, i_{cirj}, and n_{cirj} are derived in Equs. (15), (16), (18), (20), and (21) to verify the calculated maximum modulation index, and the simulation results are shown in Fig. 6. The MMC must be operated in the condition with a power factor of $\sqrt{3}/2$, which is the worst case. For this case, the modulation signal starts to hit the limit of M = 0.92. Fig. 7 shows the upper (lower) arm current with different modulation indices. The upper (lower) current is in normal operation when M = 0.90, and the modulation signal is close to 1. However, this signal has some notches and also exceeds the rated current value when M = 0.95. Meanwhile, the modulation signal exceeds 1. This phenomenon is called overmodulation. The simulation results verify the theoretical analysis on the maximum modulation index limitation.

As mentioned, n_{cir} is related to the frequency characteristics in Equ. (31). The DC terminal output voltage and current can be monitored with frequency sweeping between 5 and 990 Hz, which can be adjusted according to the studied bandwidth. The DC impedance can also be derived by applying Fourier decomposition. The frequency domain analysis result of DC-side impedance is shown in Fig. 8. The equivalent circuit and simulation results without and with circulating current

TABLE I
Parameters of MMC-HVDC

Parameters	Value
Rated power of MMC-HVDC	250 MVA
Rated AC voltage of MMC	161 kV
Rated DC voltage of MMC	300 kV
Number of SM of each arm	200
Inductance of each arm	24.7 mH
Capacitance of each SM	10 mF
DC cable length	100 km
DC cable resistance	0.0132 Ω/km
DC cable inductance	3.06×10^{-4} H/km
DC cable capacitance	3.3×10^{-7} F/km
Switching frequency	500 Hz
Smoothing reactor	41.5 mH

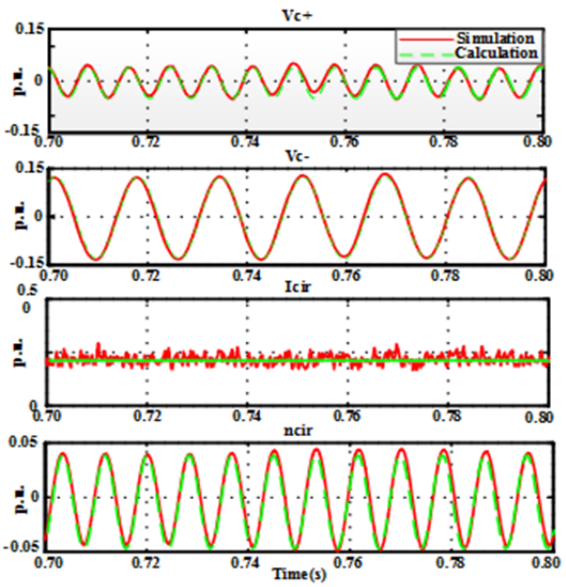

Fig. 6. Steady-state simulation results of MMC-HVDC.

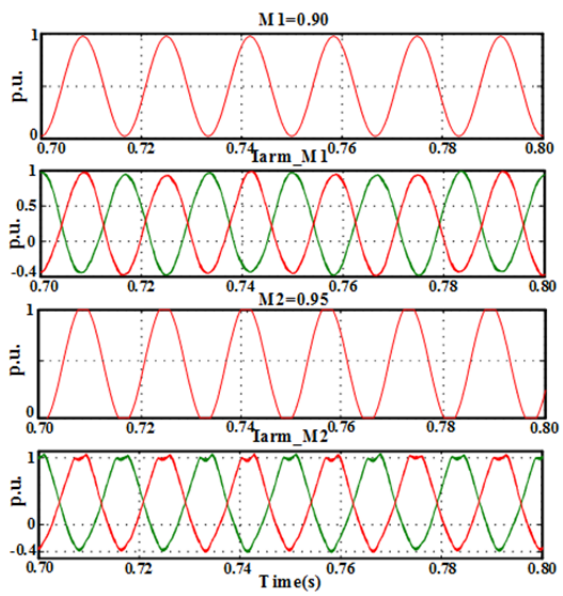

Fig. 7. Upper (lower) arm current under different modulation indices of MMC.

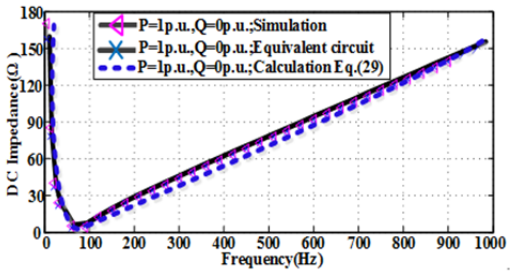

(a) Without $n_{cir.}$

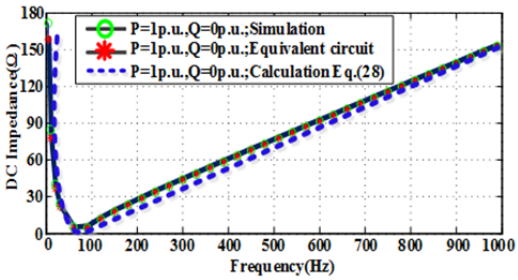

(b) With $n_{cir.}$

Fig. 8. DC impedance frequency characteristic.

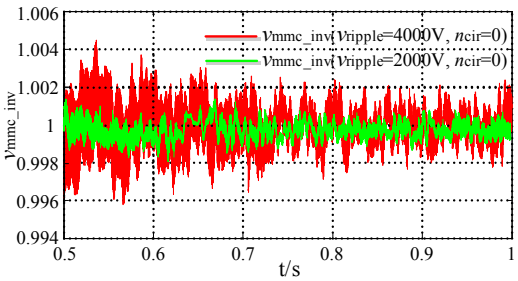

(a) Different voltage ripple values for v_{mmc_inv}.

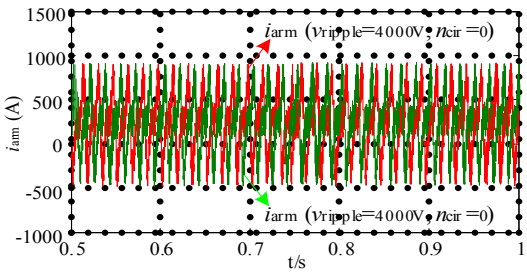

(b) Different voltage ripple values for $i_{arm.}$

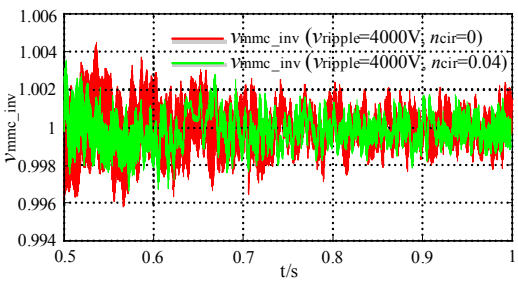

(c) Different compensating component indices for v_{mmc_inv}.

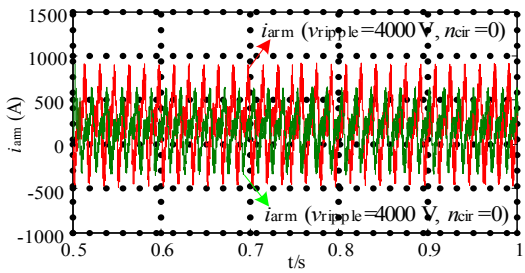

(d) Different compensating component indices for $i_{arm.}$

Fig. 9. Effect of system parameters for DC voltage ripple transfer and upper or lower arm current.

control closely match the theoretical analysis from Equs. (31) and (32), and n_{cir} has a small effect on the DC-side impedance frequency characteristics.

The simulation results in fault condition are shown in Fig. 9 when the oscillation in the DC voltage occurs in the rectifier side of the system and is transferred to the inverter side. Fig. 9(a) illustrates that when the fault voltage is 4000 or 2000 V and n_{cir} = 0, transferring through the power cable with the same parameters and high oscillation in the inverter stage can be determined at the ending terminal with high oscillation in the starting terminal. Fig. 9(b) illustrates that a similar upper or lower arm current can be detected in the inverter side under the same case.

The DC voltage ripple with a minimal value is shown in Fig. 9(c) when the voltage ripple value is fixed and the compensating component of modulation index is added. However, the upper or lower arm current is reduced in Fig. 9(d). Hence, the effect of injecting compensated terms into the modulation index is higher on the bridge current than on voltage fluctuation.

B. Experiment Verifications

To verify the preceding analysis, a 1 kW downscaled three-phase MMC prototype was built. The prototype consists of 2 SMs per arm, and the rated DC voltage is 100 V. The SM capacitance is 2700 μF, and the arm inductance is 0.5 mH. The carrier frequency is 1 kHz. The load resistance is 5 Ω. The DC-side inductance is 0.5 mH, and AC-side inductance is 1.5 mH. A single full-bridge converter is used to generate voltage ripple into the DC side of the rectifier in the two-terminal MMC-HVDC system.

Fig. 10 illustrates the experimental results for the worst case when the power factor is $\sqrt{3}/2$ and M is 0.92, which is the critical value. The circulating current has some small notches when the modulation index reached the maximum value. This phenomenon occurs because of overmodulation, and a theoretical analysis is discussed in Section III.

Fig. 11 shows the experimental results of the upper and lower arm currents and the inverter side voltage ripple for the MMC-HVDC system when the rectifier-side voltage ripple v_{ripple} is 5 V and the circulating current compensating component n_{cir} is 0. Given that the voltage ripple is transferred from the DC side of the rectifier, the second-order

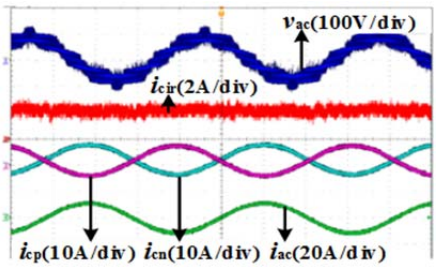

Fig. 10. Experimental results with cosφ = $\sqrt{3}/2$ and M = 0.92.

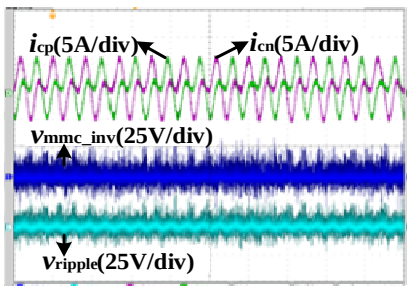

Fig. 11. DC voltage ripple transfer component and arm current with n_{cir} = 0 and v_{ripple} = 5 V.

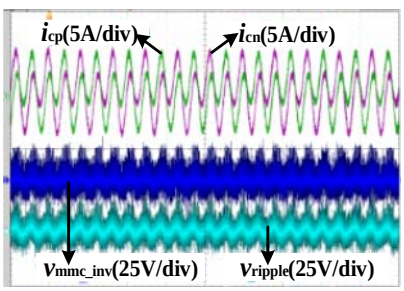

Fig. 12. DC voltage ripple transfer component and arm current with n_{cir} = 0, v_{ripple} = 10 V.

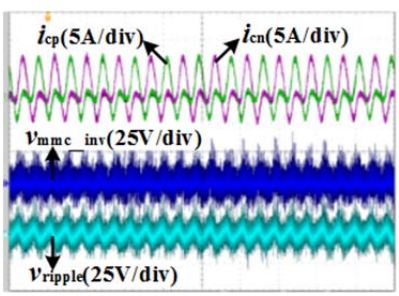

Fig. 13. DC voltage ripple transfer component and arm current with n_{cir} = 0.04, v_{ripple} = 10 V.

harmonics appears at the DC side of the inverter for MMC-HVDC.

Results of the voltage ripple in the DC side of the inverter and upper and lower arm currents when v_{ripple} is increased to 10 V are shown in Fig. 12. Unlike Fig. 11, Fig. 12 illustrates that the arm current and the inverter-side DC voltage ripple increase obviously with a large voltage ripple and without a compensating component (n_{cir} = 0).

Fig. 13 shows that the voltage ripple is the same as that in Fig. 12, which is kept as 10 V. The compensating component n_{cir} = 0.04 is introduced in the modulation index. Unlike that in Fig. 12, the voltage ripple in Fig. 13 does not change significantly. However, the circulating current in Fig. 13 becomes considerably smaller than that in Fig. 12. Therefore, a high-voltage ripple leads to an increased voltage ripple that transfers from one side to the other, and the compensating component in the modulation index leads to decreased arm currents.

VI. Conclusion

A DC-side equivalent impedance model in frequency domain that describes the analytical expression in MMC-HVDC systems simply and accurately is proposed. On the basis of this model, the influences of DC cable and inverter parameters on DC voltage ripple distribution are analyzed in detail under unbalanced conditions according to an analysis of simulation results and experimental verifications. The following can be concluded:

1) Compensating component n_{cir} reduces the converter maximum modulation index, which affects the DC voltage utilization. It is also related to SM capacitance.
2) DC-side impedance can be represented with *R*, *L*, and *C* in series when the compensating component n_{cir} is not applied.
3) The main trends of the DC-side impedance characteristics are nearly the same with/without compensating component n_{cir} of NLM.
4) The unbalanced fault occurs at the rectifier of the two-terminal MMC-HVDC system. Its effect on the inverter has been studied with the DC-side impedance model.

References

[1] J. M. Carrasco, L. G. Franquelo, J. T. Bialasiewicz, and E. Galvan, "Power-electronic systems for the grid integration of renewable energy sources: A survey, " *IEEE Trans. Ind. Electron.*, Vol. 53, No. 4, pp. 1002-1016, Jun. 2006.

[2] K. Shen, D. Zhao, J. Mei, and L. M. Tolbert. "Elimination of harmonics in a modular multilevel converter using particle swarm optimization-based staircase modulation strategy," *IEEE Trans. Ind. Electron.,* Vol. 61, No. 10, pp. 5311-5322, Oct. 2014.

[3] P. M. Meshram and V. B. Borghate, "A simplified nearest level control (NLC) voltage balancing method for modular multilevel converter (MMC)," *IEEE Trans. Power Electron.*, Vol. 30, No. 1, pp. 450-462, Jan. 2015.

[4] M. Glinka and R. Marquardt. "A new ac/dc multilevel converter family," *IEEE Trans. Ind. Electron.,* Vol. 52, No. 3, pp. 662-669, 2005.

[5] Q. R. Tu and Z. Xu, "Impact of sampling frequency on harmonic distortion for modular multilevel converter," *IEEE Trans. Power Del.,* Vol. 26, No. 1, pp. 298-306, Jan. 2011.

[6] K. Ilves, A. Antonopoulos, S. Norrga, H.-P. Nee, "Steady-state analysis of interaction between harmonic

components of arm and line quantities of modular multilevel converters," *IEEE Trans. Power Electron.*, Vol. 27, No. 1, pp. 57-68, Jan. 2012.
[7] Y. L. Li, E. A. Jones, and F. Wang. "Analysis of the relationship between switching frequency and sub-module capacitor unbalanced voltage for a modular multilevel converter," in *Proc. Applied Power Electronics Conference and Exposition(APEC),* pp. 220-224, Mar. 2014.
[8] M. Y. Guan and Z. Xu. "Modeling and control of a modular multilevel converter-based HVDC system under unbalanced grid conditions," *IEEE Trans. Power Electron.*, Vol. 27, No. 12, pp. 4858-4867, Dec. 2012.
[9] J.-W. Moon, C.-S. Kim, J.-W. Park, and D.-W. Kang, "Circulating current control in MMC under the unbalanced voltage," *IEEE Trans. Power Del.*, Vol. 28, No. 3, pp. 1952-1959, Jul. 2013.
[10] Q. R. Tu, Z. Xu, and L. Xu. "Reduced switching-frequency modulation and circulating current suppression for modular multilevel converters," *IEEE Trans. Power Del.*, Vol. 26, No. 3, pp. 2009-2017, Jul. 2013.
[11] S. H. Li, X. L. Wang, Z. Q. Yao, T. Li, and Z. Peng, "Circulating current suppressing strategy for MMC-HVDC based on nonideal proportional resonant controllers under unbalanced grid conditions," *IEEE Trans. Power Electron.*, Vol. 30, No. 1, pp. 387-397, Jan. 2015.
[12] M. Hagiwara and H. Akagi, "Control and experiment of pulse width modulated modular multilevel converters," *IEEE Trans. Power Electron.,* Vol. 24, No. 7, pp. 1737-1746, Jul. 2009.
[13] S. Rohner, S. Bernet, M. Hiller, and R. Sommer, "Modulation, losses, and semiconductor requirements of modular multilevel converters," *IEEE Trans. Ind. Electron.,* Vol. 57, No. 8, pp. 2633–2642, Aug. 2010.
[14] D. C. Ludois and G. Venkataramanan, "Simplified terminal behavioral model for a modular multilevel converter," *IEEE Trans. Power Electron.,* Vol. 29, No. 4, pp. 1622-1631, Apr. 2014.
[15] P. F. Hu and D. Z. Jiang, "A level-increased nearest level modulation method for modular multilevel converters," *IEEE Trans. Power Electron.,* Vol. 30, No. 4, pp.1836-1842, Apr. 2015.
[16] Q. Song, W. H. Liu, X. Q. Li, and H. Rao, "A steady-state analysis method for a modular multilevel converter," *IEEE Trans. Power Electron.,* Vol. 28, No. 8, pp. 3702-3713, Aug. 2013.
[17] X. J. Shi, Z. Q. Wang, B. Liu, Y. Q. Liu, L. M. Tolbert, and F. Wang, "Characteristic investigation and control of a modular multilevel converter-based HVDC system under single-line-to-ground fault conditions," *IEEE Trans. Power Electron.,* Vol. 30, No. 1, pp. 408-421, Jan. 2015.
[18] Q. R. Tu, Z. Xu, Y. Chang, and L. Guan, "Suppressing DC voltage ripples of MMC-HVDC under unbalanced grid conditions," *IEEE Trans. Power Del.,* Vol. 27, No. 3, pp. 1332-1338, Jul. 2012.
[19] J.-W. Moon, C.-S. Kim, J.-W. Park, D.-W. Kang, and J.-M. Kim, "Circulating current control in MMC under the unbalanced voltage," *IEEE Trans. Power Del.,* Vol. 28, No. 3, pp. 1952-1959, Jul. 2013.
[20] Y. L. Li, E. A. Jones, and F. Wang, "Switching- frequency ripple in dc link voltage in a modular multilevel converter with circulating current suppressing control," in *Proc. Applied Power Electronics Conference and Exposition(APEC),* pp. 191-195, Mar. 2014.
[21] K. Ilves, A. Antonopoulos, S. Norrga, and H.-P. Nee, "A new modulation method for the modular multilevel converter allowing fundamental switching frequency," *IEEE Trans. Power Electron.,* Vol. 27, No. 8, pp. 3482-3494, Aug. 2012.
[22] Michail Vasiladiotis, "Analysis, implementation and experimental evaluation of control systems for a modular multilevel converter," *PhD thesis, Royal Institute of Technology*, 2009.
[23] ABB, *It's time to connect with offshore wind supplement*, http://www.abb.com/ hvdc, 2013.
[24] X. N. Lu, J. M. Guerrero, K. Sun, and J. C. Vasquez, "An improved droop control method for DC microgrids based on low bandwidth communication with dc bus voltage restoration and enhanced current sharing accuracy," *IEEE Trans. Power Electron.*, Vol. 29, No. 4, pp. 1800-1812, Apr. 2014.
[25] X. N. Lu, K. Sun, J. M. Guerrero, J. C. Vasquez, and L. P. Huang, "Double-quadrant state-of-charge-based droop control method for distributed energy storage systems in autonomous DC microgrids," *IEEE Trans. Smart Grid*, Vol. 6, No. 1, pp. 147-157, Jan. 2015.

Yiqi Liu received his B.S. degree in Electrical Engineering from Northeast Agriculture University, Harbin, China, in 2009. He received his M.S. degree in Electrical Engineering from Tianjin University of Technology, Tianjin, China, in 2012. He is currently working toward his Ph.D. degree in the School of Electrical Engineering and Automation at the Harbin Institute of Technology, Harbin, China. From 2013 to 2015, he was a visiting Ph.D. student at the Center for Ultra-Wide-Area Resilient Electric Energy Transmission Networks, The University of Tennessee, Knoxville, Tennessee, USA, supported by the China Scholarship Council. His current research interests include power electronics for renewable energy sources, multilevel converter, high-voltage DC technology, DC microgrid, and energy conversion.

Qichao Chen received the M.S. degree in electrical engineering from Harbin Institute of Technology, Harbin, China, in 2009, and the Ph.D. degree from the Harbin Institute of Technology, Harbin, China, in 2015.
His research interests include power electronic transformer for renewable energy systems, as well as bus power flow controller for hybrid ac/dc distribution, high efficiency isolation bidirectional DC/DC converter, battery energy storage systems, and photovoltaic generation.

Ningning Li received his B.S. and M.S. degrees in Electronics Engineering from Northeast Agriculture University, Harbin, China, in 2005 and 2010, respectively. He is currently working toward his Ph.D. degree in the School of Electrical Engineering and Automation at the Harbin Institute of Technology, Harbin, China. His current research interests include power electronics and drives, renewable energy generation and applications, FACTS, and power quality.

Bing Xie received his B.S. and M.S. degrees in Electrical Engineering from Shenyang Agriculture University, Shenyang, China, in 2008 and 2013, respectively. He is currently working toward his Ph.D. degree in the School of Electrical Engineering and Automation at the Harbin Institute of Technology, Harbin, China. His current research interests include renewable energy sources technology, FATCS, and energy storage technology.

Jianze Wang received his B.S., M.S., and Ph.D. degrees in Electrical Engineering from the Harbin Institute of Technology, Harbin, China, in 1993, 1996, and 1999, respectively. He joined the Harbin Institute of Technology in 1999, where he is currently a research professor. From July 2003 to December 2003, he was a visiting scholar at the Hong Kong Polytechnic University, Hong Kong. His current research interests include power electronics, multilevel converters, and digital signal processor-based power quality control systems.

Yanchao Ji received his B.S. and M.S. degrees in Electrical Engineering from Northeast Dianli University, Jilin, China, in 1983 and 1989, respectively. He received his Ph.D. degree in Electrical Engineering from North China Electric Power University, Beijing, China, in 1993. He joined the Department of Electrical Engineering of the Harbin Institute of Technology, Harbin, China, in 1993. From 1995 to 1996, he was an associate professor at the Department of Electrical Engineering of the Harbin Institute of Technology, where he is currently a professor. His current research interests include pulse width modulation technique, power converter, and flexible AC transmission system devices.